Determination of Unfiltered Radiances from the Clouds and the Earth's Radiant Energy System Instrument

NORMAN G. LOEB

Center for Atmospheric Sciences, Hampton University, Hampton, Virginia

KORY J. PRIESTLEY, DAVID P. KRATZ, ERIKA B. GEIER, RICHARD N. GREEN, AND BRUCE A. WIELICKI

NASA Langley Research Center, Hampton, Virginia

PATRICIA O'RAWE HINTON AND SANDRA K. NOLAN

Science Applications International Corporation, Hampton, Virginia

(Manuscript received 17 May 2000, in final form 18 September 2000)

ABSTRACT

A new method for determining unfiltered shortwave (SW), longwave (LW), and window radiances from filtered radiances measured by the Clouds and the Earth's Radiant Energy System (CERES) satellite instrument is presented. The method uses theoretically derived regression coefficients between filtered and unfiltered radiances that are a function of viewing geometry, geotype, and whether cloud is present. Relative errors in instantaneous unfiltered radiances from this method are generally well below 1% for SW radiances (std dev ≈0.4% or ≈1 W m^{-2} equivalent flux), less than 0.2% for LW radiances (std dev ≈0.1% or ≈0.3 W m^{-2} equivalent flux), and less than 0.2% (std dev ≈0.1%) for window channel radiances.

When three months (June, July, and August of 1998) of CERES Earth Radiation Budget Experiment (ERBE)-like unfiltered radiances from the *Tropical Rainfall Measuring Mission* satellite between 20°S and 20°N are compared with archived *Earth Radiation Budget Satellite* (ERBS) scanner measurements for the same months over a 5-yr period (1985–89), significant scene-type dependent differences are observed in the SW channel. Full-resolution CERES SW unfiltered radiances are ≈7.5% (≈3 W m^{-2} equivalent diurnal average flux) lower than ERBS over clear ocean, as compared with ≈1.7% (≈4 W m^{-2} equivalent diurnal average flux) for deep convective clouds and ≈6% (≈4–6 W m^{-2} equivalent diurnal average flux) for clear land and desert. This dependence on scene type is shown to be partly caused by differences in spatial resolution between CERES and ERBS and by errors in the unfiltering method used in ERBS. When the CERES measurements are spatially averaged to match the ERBS spatial resolution and the unfiltering scheme proposed in this study is applied to both CERES and ERBS, the ERBS all-sky SW radiances increase by ≈1.7%, and the CERES radiances are now consistently ≈3.5%–5% lower than the modified ERBS values for all scene types. Further study is needed to determine the cause for this remaining difference, and even calibration errors cannot be ruled out. CERES LW radiances are closer to ERBS values for individual scene types—CERES radiances are within ≈0.1% (≈0.3 W m^{-2}) of ERBS over clear ocean and ≈0.5% (≈1.5 W m^{-2}) over clear land and desert.

1. Introduction

Global, top-of-atmosphere (TOA) observations of the incoming solar and outgoing terrestrial fluxes are needed to accurately determine the earth's radiation budget. The most comprehensive experiment to date to produce such measurements is the Earth Radiation Budget Experiment (ERBE; Barkstrom 1984; Barkstrom and Smith 1986). ERBE involved broadband scanning and nonscanning radiometers aboard the *Earth Radiation Budget Satellite* (ERBS), *NOAA-9,* and *NOAA-10.* The ERBE scanning instruments consisted of a total channel (TOT), measuring radiation from 0.2 to greater than 50 μm, a shortwave channel (SW) between 0.2 and 5 μm, and a longwave channel (LW) between 5 and 50 μm. To recognize the important role of clouds on the earth's radiation budget, the Clouds and the Earth's Radiant Energy System (CERES) experiment was established to provide comprehensive datasets of coincident cloud and radiation budget data using a multisatellite, multiple-instrument approach (Wielicki et al. 1996). In addition to having SW and TOT channels, CERES has a window channel (WN) (8–12 μm) for improved estimates of

Corresponding author address: Dr. Norman G. Loeb, Mail Stop 420, NASA Langley Research Center, Hampton, VA 23681-0001.
E-mail: n.g.loeb@larc.nasa.gov

surface and atmospheric radiative fluxes and to provide a means of separating window and nonwindow atmospheric greenhouse effects. Cloud properties are determined based on coincident, high-resolution imager measurements.

Several steps are required to produce monthly regional TOA fluxes from raw ERBE or CERES measurements. Radiation received by an instrument viewing the earth from a given sun–earth–satellite configuration must first be converted from digital counts to calibrated ''filtered'' radiances. Because filtered radiances are dependent upon how the radiation is filtered through the instrument optics, a procedure is applied that corrects for the imperfect spectral response of the instrument. This produces ''unfiltered'' radiances that represent the radiation received by the instrument prior to entering the optics. TOA fluxes are estimated using empirically derived anisotropic or angular distribution models (ADMs) that convert unfiltered radiances to instantaneous radiative fluxes. A major improvement in CERES ADM development is the availability of coincident CERES measurements with imager-derived cloud properties (Wielicki et al. 1996; Loeb et al. 1999). The approach for determining regional monthly mean fluxes is described in Young et al. (1998). Other CERES products, such as surface and atmospheric fluxes and cloud properties, are described in Wielicki et al. (1996).

This paper describes the methodology used to determine unfiltered radiances from CERES measurements. In the following, the unfiltering algorithm and the associated spectral radiance database are described, followed by an error analysis based on theoretical test cases. Next, a detailed statistical comparison of SW and LW radiances between CERES on the *Tropical Rainfall Measuring Mission* (TRMM) and ERBS is presented using three months (June, July, and August) of CERES and 5 yr of ERBS measurements for the same months. Last, the relationship between WN and LW nighttime radiances derived from CERES measurements and from line-by-line radiative transfer model calculations is examined.

2. Methodology

a. Filtered radiances

Radiation from earth scenes is collected and focused by primary and secondary mirrors. The radiation passes through the spectral filter, impinges on the detector, and causes a signal that is sampled and processed by the electronics. The three CERES detectors are coaligned and mounted on a spindle that rotates about the elevation axis. The fields of view for the separate channels overlap each other by approximately 98%. CERES detector output signals are fed into the telemetry stream as voltages, which are converted into digital counts. Radiometric count conversion algorithms convert the detector digital counts into filtered radiances, using calibration (count conversion) coefficients (Priestley et al. 2000) that are derived in ground laboratory measurements.

At the present time, CERES instruments aboard the TRMM and *Terra* satellites are in operation. Two more CERES instruments are scheduled to fly on the Aqua satellite starting in 2001. Based on 8 months of available TRMM observations, the CERES instrument has shown a consistency of $\approx$0.25% between in-orbit and ground calibration. A more detailed description of the procedure for determining CERES filtered radiances and a summary of its first year of operation is provided in Priestley et al. (2000).

b. Unfiltering algorithm

For use in science applications, radiances from earth scenes should be independent of the optical path in the instrument. Furthermore, because radiation escaping the earth's TOA is predominantly in the form of reflected solar and emitted thermal energy, it is desirable to separate radiance measurements unambiguously according to these categories across the spectrum. Measured filtered radiances must thus be unfiltered, or equivalently, corrected for the imperfect spectral response of the instrument. This section describes an algorithm to convert measured CERES filtered radiances to unfiltered radiances.

Unfiltered reflected SW and emitted LW and WN radiances are defined as follows:

$$m_u^{\mathrm{SW}} = \int_0^\infty I_\lambda^r \, d\lambda, \tag{1a}$$

$$m_u^{\mathrm{LW}} = \int_0^\infty I_\lambda^e \, d\lambda, \quad \text{and} \tag{1b}$$

$$m_u^{\mathrm{WN}} = \int_{\lambda_1}^{\lambda_2} I_\lambda^e \, d\lambda, \tag{1c}$$

where λ (μm) is the wavelength, and I_λ^r and I_λ^e (W m^{-2} sr^{-1} μm^{-1}) represent the reflected solar and emitted thermal radiances, respectively. For CERES, the unfiltered WN radiance m_u^{WN} is defined over a wavelength interval of $\lambda_1 = 8.1$ μm and $\lambda_2 = 11.8$ μm. The unfiltered radiances are determined from the measured filtered radiances, which can be modeled as

$$m_f^j = \int_0^\infty S_\lambda^j I_\lambda \, d\lambda, \tag{2}$$

where S_λ^j is the spectral response function ($0 \le S_\lambda^j \le 1.0$); I_λ (W m^{-2} sr^{-1} μm^{-1}) is the spectral radiance incident on the instrument ($=I_\lambda^r + I_\lambda^e$); and j denotes the SW, TOT, or WN channel. The spectral response functions for the CERES–TRMM detectors are shown in Fig. 1a. These functions represent the spectral throughput of the individual detector optical elements determined from laboratory measurements (Priestley et al.

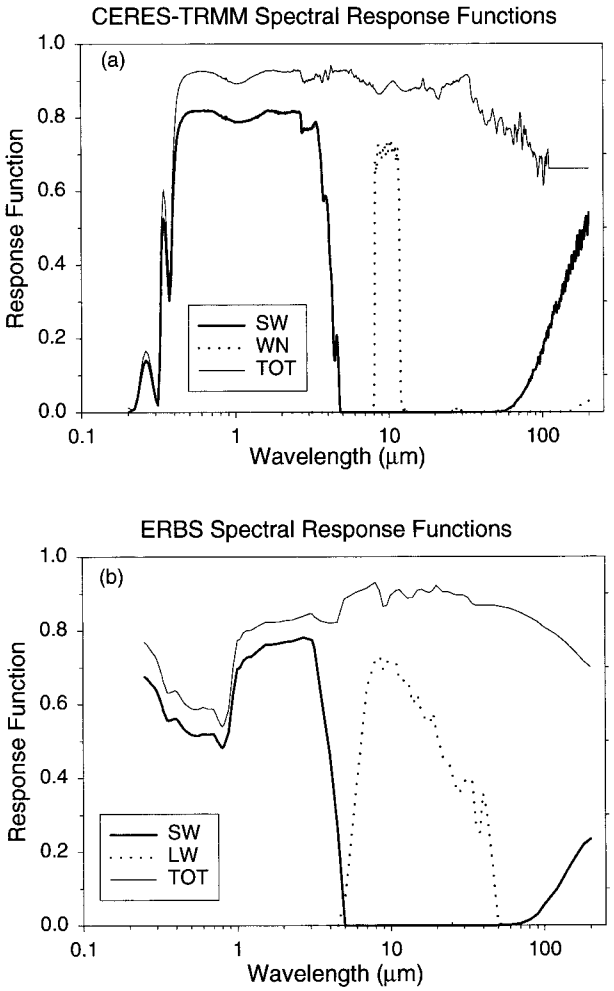

FIG. 1. Spectral response functions for (a) CERES–TRMM and (b) ERBS.

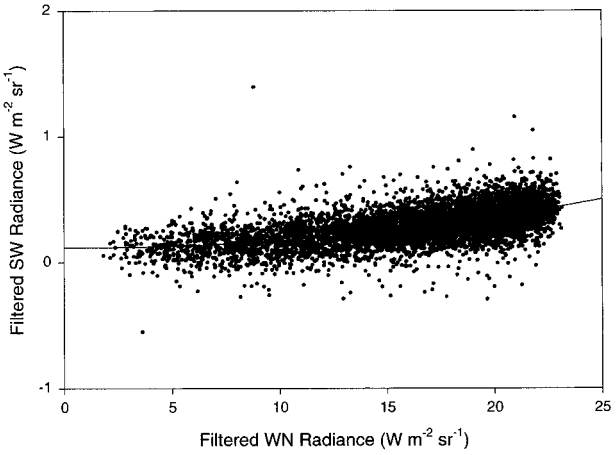

FIG. 2. Filtered SW against filtered WN radiance measurements at night from 6 days of CERES–TRMM measurements between Jan and Apr of 1998. Solid line corresponds to second-order polynomial fit defined in Eq. (4).

1998). For comparison, Fig. 1b shows spectral response functions for the ERBS instrument. CERES–TRMM spectral response functions have a higher throughput and a flatter response over more of the spectrum when compared with ERBS. An exception occurs in the ultraviolet region between 0.3 and 0.4 μm, where the CERES spectral response function exhibits a large decrease. Differences between the CERES and ERBS spectral response functions are due to the different mirrors on the two instruments—CERES uses silvered primary and secondary mirrors, and aluminum mirrors were used on ERBE.

Unfiltered reflected SW radiances m_u^{SW} and emitted WN radiances m_u^{WN} are determined from the filtered radiance measurements as follows:

$$m_u^{\mathrm{SW}} = a_0 + a_1(m_f^{\mathrm{SW}_r}) + a_2(m_f^{\mathrm{SW}_r})^2 \quad \text{and} \tag{3}$$

$$m_u^{\mathrm{WN}} = b_0 + b_1(m_f^{\mathrm{WN}}) + b_2(m_f^{\mathrm{WN}})^2, \tag{4}$$

where a_0, a_1, a_2, b_0, b_1, and b_2 are theoretically derived regression coefficients that depend on scene type and viewing geometry. Here, $m_f^{\mathrm{SW}_r}$ represents the reflected portion of the filtered SW radiance measurement and is given by

$$m_f^{\mathrm{SW}_r} = m_f^{\mathrm{SW}} - m_f^{\mathrm{SW}_e}, \tag{5}$$

where $m_f^{\mathrm{SW}_e}$ is the emitted thermal portion of m_f^{SW} and is estimated from m_f^{WN} using a predetermined empirical second-order polynomial expression relating nighttime m_f^{SW} and m_f^{WN} measurements. This relationship is shown in Fig. 2 based on 6 days of CERES–TRMM measurements. The least squares fit is given by

$$m_f^{\mathrm{SW}_e} = k_0 + k_1(m_f^{\mathrm{WN}}) + k_2(m_f^{\mathrm{WN}})^2, \tag{6}$$

where $k_0 = 0.120\,781$, $k_1 = -0.001\,696\,59$, and $k_2 = 0.000\,687\,465$. Note that because the reflected solar contribution is negligible in the window region, m_f^{WN} in Eq. (4) is assumed to consist entirely of emitted thermal radiation for both daytime and nighttime conditions.

As for ERBE, the CERES unfiltered emitted LW radiance is determined from measurements in the other channels. Here we use expressions of the form

$$m_u^{\mathrm{LW}}(D) = c_0 + c_1 m_f^{\mathrm{SW}_r} + c_2 m_f^{\mathrm{TOT}} + c_3 m_f^{\mathrm{WN}} \quad \text{and}$$

$$m_u^{\mathrm{LW}}(N) = d_0 + d_1 m_f^{\mathrm{TOT}} + d_2 m_f^{\mathrm{WN}}, \tag{7}$$

where c_0, c_1, c_2, c_3, d_0, d_1, and d_2 are theoretically derived regression coefficients, and D and N denote daytime and nighttime, respectively.

Regression coefficients in Eqs. (3), (4), and (7) are obtained from a regression analysis of theoretically derived filtered and unfiltered radiances in each channel. The simulated radiances are inferred from a spectral radiance database of typical earth scenes and the spectral response functions in Fig. 1. To determine $m_f^{\mathrm{SW}_r}$ in these simulations, I_λ in Eq. (2) is replaced with I_λ^r.

TABLE 1. Regression coefficient angular bin definitions (°).

Solar zenith angle	Viewing zenith angle	Relative azimuth angle
0.0–22.2	0.0–15.0	0–15.0
22.2–41.4	15.0–30.0	15.0–60.0
41.4–60.0	30.0–45.0	60.0–120.0
60.0–75.5	45.0–60.0	120.0–165.0
75.5–85.0	60.0–90.0	165.0–180.0

TABLE 2. Scene types for which regression coefficients are determined.

Channel	Ocean	Land or desert	Snow
SW	Clear, cloud	Clear, cloud	All
LW	All	All	All
WN	All	All	All

c. Spectral radiance database

The spectral nature of representative earth scenes is determined from high-spectral-resolution radiative transfer model calculations using measured input parameters characteristic of earth scenes. The spectral radiance database is determined from two radiative transfer codes, moderate-resolution transmittance model (MODTRAN 3.7; Kneizys et al. 1996) and discrete ordinate radiative transfer (DISORT; Stamnes et al. 1988). Window channel and TOT (N) radiances are computed at a spectral resolution of 2 cm^{-1} in intervals of 2 cm^{-1}, and SW and TOT (D) channels are computed at a spectral resolution of 20 cm^{-1} in intervals of 10 cm^{-1}. Eight streams are used in the DISORT calculations. Increasing the number of streams in the calculations to 64 was found to have a negligible effect on the unfiltering algorithm ($<0.02\%$ difference in unfiltered:filtered radiance ratios, even for thick overcast clouds). Unfiltered radiances are determined by integrating spectral radiances over the appropriate wavenumber interval using Gaussian quadrature (5000 quadrature points are used). In a similar way, filtered radiances are computed by integrating over the product of spectral radiance and spectral response function. The regression coefficients are evaluated at 125 angles (5 solar zenith; 5 viewing zenith; 5 relative azimuth) for the angles shown in Table 1.

Scene-type categories used in the unfiltering algorithm are defined in Table 2 for each channel. Three geotype categories (ocean, land and desert, and snow) are considered. The shortwave channel is further subdivided into clear and cloudy categories. Spectral radiances from 119 scenes were used to represent ocean, 102 were used for land or desert, and 51 were used for snow. The oceanic spectral radiance calculations assumed a tropical atmospheric profile (McClatchey et al. 1972) and a maritime aerosol model (Shettle and Fenn 1979). MODTRAN was modified to allow for a rough ocean surface based on Takashima (1985), which uses the Cox and Munk (1954) approach for simulating ocean surface roughness. Table 3 shows the 0.55-μm aerosol and cloud optical depths, surface temperatures, and cloud types used to represent cloud-free and overcast oceanic scenes. Radiances from broken clouds were determined for cloud fractions of 0.25, 0.50, and 0.75 by linearly weighting cloud-free and overcast filtered and unfiltered radiances for all combinations of cloud-free and overcast scenes. Table 4 summarizes the atmospheric profiles, aerosols, surface types, and surface temperatures considered for the cloud-free calculations over land and desert. The atmospheric profiles are from McClatchey et al. (1972); aerosol models are based on Shettle and Fenn (1979). References for the surface spectral albedo are provided in Table 4. Cloud spectral radiances over the land surfaces are computed for each surface type using the same cloud conditions as in Table 3 for ocean. Scene properties for calculating spectral radiances over snow are shown in Table 5. In all cases, a subarctic winter profile (McClatchey et al. 1972) and tropospheric aerosol model (Shettle and Fenn 1979) is assumed. Surface albedos are determined using the Wiscombe and Warren (1980) snow albedo model for three snow grain sizes ($r_g = 50$ μm; $r_g = 200$ μm, and $r_g = 1000$ μm). The overcast cloud models for subvisual cirrus, cirrus, stratus, and stratocumulus are based on Silverman and Sprague (1970).

3. Error analysis

To test the unfiltering algorithm, theoretical filtered and unfiltered radiances computed for surface and atmospheric conditions different from those used to generate the regression coefficients in Eqs. (3), (4), and (7) are considered. Applying the unfiltering algorithm to these cases and comparing estimated unfiltered radiances with the ''true'' calculated values provides an estimate of the error in the unfiltering procedure. Tables 6 and 7 show the conditions used to test the unfiltering algorithm. Note that the same overcast conditions (Table 6) were used over ocean and land. Over ocean, a total of 1541 test cases were considered, and 10 940 cases were considered over land.

TABLE 3. Summary of cloud-free and overcast properties used in radiative transfer calculations for oceanic conditions.

Optical depth (at 0.55 μm)	Surface temperature (K)	Cloud
0	320	–
0.055	310	–
0.09	300	–
0.161	295	–
0.301	290	–
0.674	285	–
1.171	280	–
4	300	Cirrus
12	300	Cirrus
14	300	Stratus
217	300	Cumulus

TABLE 4. Summary of cloud-free properties used in radiative transfer calculations for land or desert conditions.

Atmosphere	Aerosol	Optical depth (at 0.55 μm)	Surface type	Surface temperature (K)
Tropical	Desert	0.14	Desert (Tarnopolskiy 1978)	310
Tropical	Desert	0.14	Dry sand (Colwell 1983)	300
Midlatitude summer	Rural	0.30	Vegetation (Colwell 1983)	295
U.S. Standard Atmosphere, 1976	Rural	0.30	Coniferous forest (Kriebel 1978)	285
U.S. Standard Atmosphere, 1976	Rural	0.30	Forest conifer species (Tarnopolskiy 1978)	280
Midlatitude winter	Rural	0.30	Dry meadows grass (Kriebel 1978)	275

Figures 3–5 show the relative error [$=(A_e - A)/A \times 100\%$, where A_e is the estimate and A is ''truth''] in the unfiltered radiance estimate against the true unfiltered radiance for the SW, LW, and WN channels. Under cloud-free conditions (Figs. 3a–d), relative errors in instantaneous SW reflectances are generally less than 1%. Over ocean (Figs. 3a,b), the largest error ($\approx$1%) occurs for the Indian Ocean Experiment (INDOEX) case, for which the aerosols are strongly influenced by anthropogenic sources with an abundance of submicron particles and relatively high levels of soot, organics, and fly ash (Satheesh et al. 1999). Cases with errors of less than -1% are found to occur over clear land (Figs. 3c,d) in extreme conditions, when aerosol optical depths exceed 1 for the rural and urban aerosol models. In Figs. 4a–d, the cloud-free results are shown together with those for broken and overcast clouds. Over ocean, relative errors remain well below 1% for all cloud cases (Figs. 4a,b). Over land (Figs. 4c,d), relative errors can be as high as $\approx$1.5% for cirrus clouds with optical depths less than 1. Figs. 5a and 5b show relative errors for LW and WN channels, respectively. Relative errors for the LW cases are generally less than $\approx$0.2% except for very cold deep convective cloud cases, for which relative errors are closer to $\approx$0.4%. Relative errors are even smaller ($<\approx$0.2%) for the WN channel. The unfiltering algorithm was also tested in various snow conditions for different atmospheric profiles, aerosol, and cloud types, snow grain sizes, and soot concentrations in snow (not shown). Relative errors in each channel were found to be similar to those obtained over ocean and land.

Because separate unfiltering regression coefficients are used in determining unfiltered SW radiances under clear and cloudy conditions, scene identification error (i.e., whether a scene is clear or cloudy) is another source of uncertainty. To provide an upper bound on how scene identification errors affect the accuracy of unfiltered SW radiances, we have modified the analysis in Fig. 4 by determining the unfiltered SW radiances for clear scenes using regression coefficients derived under cloudy conditions, and the unfiltered SW radiances for cloudy scenes using regression coefficients derived under clear conditions. This is equivalent to the case where scene identification errors occur 100% of the time. Results in Fig. 6 show that the largest errors (reaching $\approx$3%) occur for the bright cloudy scenes, and remain less than 2% for clear scenes. Because most scene identification schemes are capable of discriminating between clear and bright cloudy scenes over ocean and land, the $<$2% bound is a more realistic estimate of the uncertainty resulting from scene identification errors.

TABLE 5. Summary of cloud-free and overcast properties used in radiative transfer calculations for snow conditions.

Optical depth (at 0.55 μm)	Snow grain size (μm)	Surface temperature (K)	Cloud
0.03	50	257	–
0.03	200	260	–
0.03	1000	270	–
0.3	All above	All above	Subvisual Cirrus
2	All above	All above	Cirrus
90	All above	All above	Stratus
4	All above	All above	Stratocumulus

4. Comparisons between CERES–TRMM and ERBS

Because instrument bias errors (e.g., due to calibration and/or offset errors) typically show little or no sensitivity to scene type (e.g., cloud cover, geotype), a scene type dependence in unfiltered radiance differences between two or more instruments is a good indicator of potential unfiltering errors. Such a comparison is particularly useful if the instruments under consideration have very different spectral response function characteristics. It would be desirable to compare coincident unfiltered radiances, but such a comparison requires instruments that are either on the same spacecraft or in very similar orbits—a situation not often realized. An alternate approach is to make a composite of several months of measurements by scene type and to compare statistically the unfiltered radiances from different instruments. This allows comparisons between any set of instruments but may be affected by other factors, such as diurnal, seasonal, and climatological changes in cloud and surface properties, instrument differences (e.g., instrument spatial resolution), and scene identification errors.

It was noted earlier that CERES–TRMM and ERBS

TABLE 6. Unfiltering algorithm test case properties for ocean.

Atmospheric profile [boundary temperature (K)]	Aerosol type (0.55-μm optical depth)	Cloud type [0.55-μm optical depth; cloud-top height (km)]
Tropical (T_b = 280–310)	None	Cumulus (τ = 217; z_t = 3)
Midlatitude summer (T_b = 270–300)	Maritime (τ = 0.02–1.0)	Stratus (τ = 38, z_t = 1)
Midlatitude winter (T_b = 250–280)	Rural (τ = 0.02–1.0)	Cirrus (τ = 0.05–30; z_t = 7–13)
Subarctic summer (T_b = 260–290)	Urban (τ = 0.02–1.0)	Subvisual cirrus (τ = 0.01–0.05; z_t = 12)
Subarctic winter (T_b = 240–270)	Desert (τ = 0.02–1.0)	Deep convection (τ = 217; z_t = 15–17)
	INDOEX (τ = 0.13)	

have very different spectral response functions (Fig. 1). In addition, there are other noteworthy differences: (i) CERES–TRMM has a footprint size of 10 km (equivalent diameter at nadir) as compared with 40 km for ERBS; (ii) ERBS measures filtered SW, LW, and TOT radiances but CERES–TRMM measures filtered SW, WN, and TOT radiances; (iii) ERBS is in a 57° inclined orbit and CERES–TRMM is in a 35° inclined orbit; (iv) the unfiltering algorithm used to determine ERBS unfiltered radiances (described in Green and Avis 1996) is very different from that described in section 2b and is based on a different spectral database [described in Arduini (1985)]. To unfilter SW radiances, the ERBE unfiltering algorithm uses a theoretical ratio between unfiltered and filtered radiances defined at various angles in overcast and cloud-free conditions over ocean, land, desert, and snow (interpolation between these theoretical ratios is used to determine coefficients under partly and mostly cloudy conditions). For CERES, a more general expression [Eq. (3)] that accounts for potential nonlinearities and nonzero intercepts in the filtered–unfiltered radiance relationship is used. To unfilter the ERBS LW channel, an expression similar to that in Eq. (7) is used in the ERBE algorithm except that the coefficients c_0, c_3, d_0, and d_2 are assumed to be zero and the LW channel replaces the WN channel. The CERES algorithm uses linear interpolation to determine radiances at angles that lie between angular bin endpoints (no angular interpolation is used for ERBS).

Because of the differences between the CERES–TRMM and ERBS spectral response functions, significant errors occur when the ERBE unfiltering approach is applied to CERES–TRMM. To illustrate, Figs. 7a–d show the theoretical ratio between unfiltered and filtered SW radiances for clear and overcast scenes over ocean and land at a solar zenith angle of 60° at nadir (the same scenes as in section 3 were used). For CERES–TRMM, this ratio shows an ≈10% variation for clear scenes over ocean and a 15% variation for overcast scenes. The variability in this ratio is much smaller for ERBS—≈2% for clear scenes and ≈4% for overcast. Over land, the ERBS unfiltering ratio is highly variable—it shows an ≈6%–8% variation in Figs. 7b and 7d as compared with ≈2%–4% for CERES–TRMM (Figs. 7a,c). Figures 7b and 7d also show the unfiltering coefficients used in the ERBE production code for the ERBS instrument (shown as horizontal lines). Of interest, the ERBS production values for clear ocean are ≈2% lower than those for the cases considered in Fig. 7b. The reason for the discrepancy is because a very large aerosol optical depth was used for clear ocean in the ERBE clear ocean spectral radiance database (Arduini 1985)—a meteorological range of 5 km was used in that database, which corresponds to a 0.55-μm aerosol optical depth of about 1. For clear land, the ERBE production unfiltering coefficient is in good agreement with the cases shown in Fig. 7b. For overcast scenes, large differences are shown in Fig. 7d, even for very thick clouds (where differences are typically ≈3%).

a. SW reflectance comparisons

Three months of CERES–TRMM unfiltered radiances from June, July, and August (JJA) of 1998 between 20°S and 20°N are compared with ERBS scanner measurements for the same months over a 5-yr period (1985–

TABLE 7. Unfiltering algorithm test case properties over clear land.

Surface	Aerosol type	Aerosol optical depths (at 0.55 μm)
Dry sand (Bowker et al. 1985)	Desert	0.0, 0.15
Dry meadows grass (Tarnopolskiy 1978)	Rural, urban	0.0, 0.16, 1.2
Conifers (JPL 1998)	Rural, urban	0.0, 0.16, 1.2
Deciduous (JPL 1998)	Rural, urban	0.0, 0.16, 1.2
Grass (JPL 1998)	Rural, urban	0.0, 0.16, 1.2
Brown silty loam (JPL 1998)	Rural, urban	0.0, 0.16, 1.2
Dark reddish brown loam (JPL 1998)	Rural, urban	0.0, 0.16, 1.2
Reddish brown loam (JPL 1998)	Rural, urban	0.0, 0.16, 1.2
Dark reddish brown silty loam (JPL 1998)	Rural, urban	0.0, 0.16, 1.2

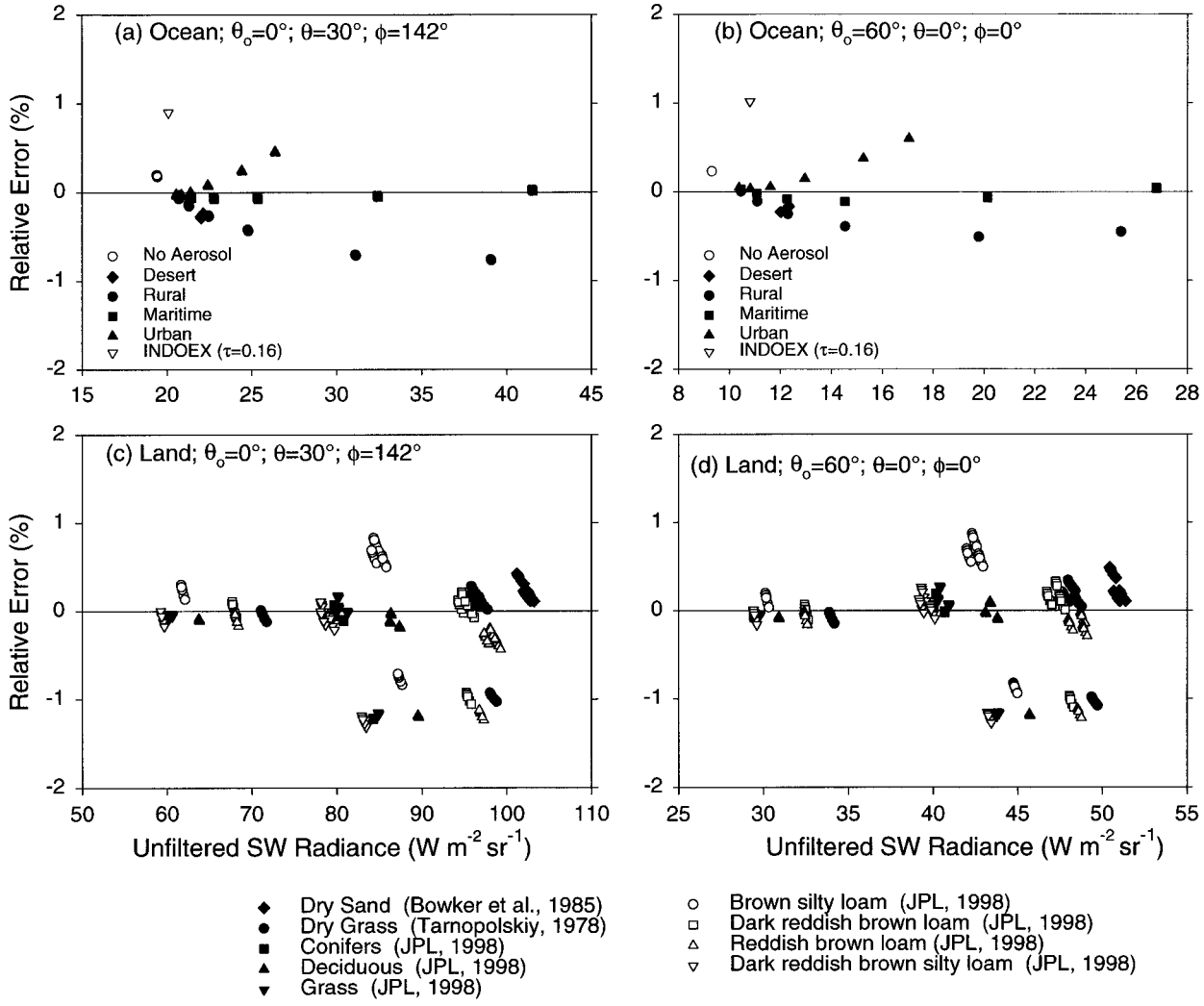

FIG. 3. Relative error in unfiltered SW radiance estimate against the true unfiltered SW radiance for (a) and (b) clear ocean and (c) and (d) clear land in two viewing geometries: (left) $\theta_0 = 0°$, $\theta = 30°$, $\phi = 142°$; (right) $\theta_0 = 60°$, $\theta = 0°$, $\phi = 0°$.

89). To minimize uncertainties due to scene identification errors, the CERES ERBE-like product is considered. Scene identification in this product is determined based on the maximum likelihood estimation technique (MLE; Wielicki and Green 1989), the same algorithm used in ERBE.

Figures 8a–c show relative frequency distributions of near-nadir (viewing zenith angles $\leq 5°$) SW reflectance for all scenes over ocean at solar zenith angles between 5° and 10° (Fig. 8a), 35° and 40° (Fig. 8b), and 65° and 70° (Fig. 8c). Reflectance (or isotropic albedo) is defined as

$$r(\theta, \theta_0, \phi) = \frac{\pi m_u^{\mathrm{SW}}(\theta, \theta_0, \phi)}{\cos(\theta_0) E_0} \times 100\%, \qquad (8)$$

where θ is the observer viewing zenith angle, θ_0 is the solar zenith angle, ϕ is the azimuth angle relative to the solar plane defined between 0° and 180° ($\phi = 0°$ corresponds to forward scattering), and E_0 is the solar irradiance (W m^{-2}) corrected for earth–sun distance. To examine how the factor of 4 difference in spatial resolution between CERES–TRMM and ERBS affects the comparisons, two sets of results are shown for CERES–TRMM: ''CERES (fullres)'' corresponds to full-resolution (10-km equivalent diameter) CERES–TRMM measurements; ''CERES (lowres)'' corresponds to spatially averaged CERES–TRMM measurements with a resolution close to that of ERBS ($\approx$40-km equivalent diameter). CERES (lowres) footprints are formed by averaging two scans of eight along-scan full-resolution CERES–TRMM footprints. In averaging the CERES footprints to match the ERBS resolution, the 95% point-spread-function of both instruments is used and footprint overlap is taken into account.

The CERES frequency distributions in Figs. 8a–c show very good agreement with those from ERBS when CERES footprints are spatially averaged [CERES (low-

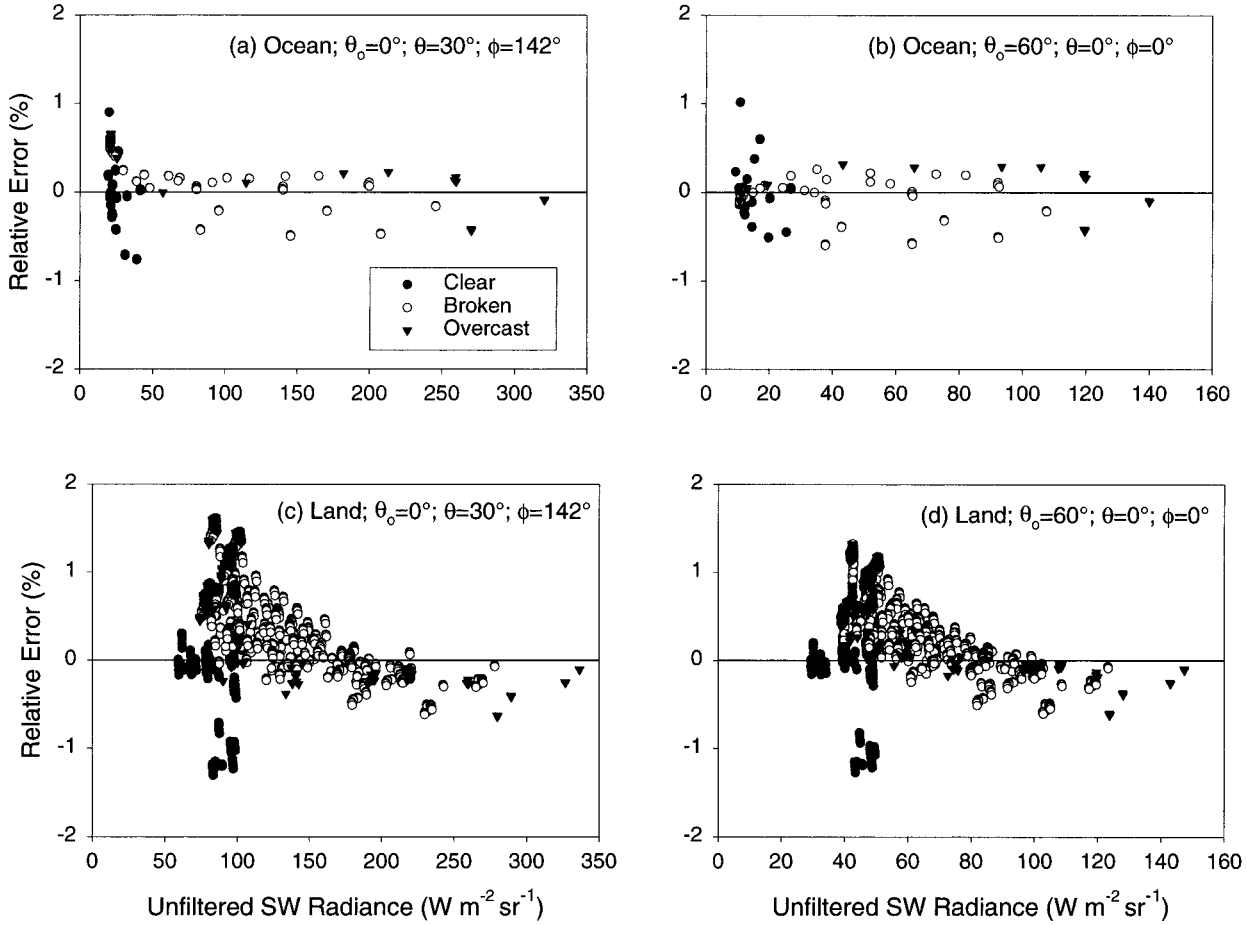

FIG. 4. Relative error in unfiltered SW radiance estimate against the true unfiltered SW radiance for clear, broken, and overcast scenes over (a) and (b) ocean and (c) and (d) land in two viewing geometries: (left) $\theta_0 = 0°$, $\theta = 30°$, $\phi = 142°$; (right) $\theta_0 = 60°$, $\theta = 0°$, $\phi = 0°$.

res)]. As CERES footprint size increases, the width of the frequency distribution increases and the peak shifts toward larger reflectances, in better agreement with ERBS. Of interest, the sensitivity of the CERES frequency distribution to footprint size also increases with solar zenith angle. Figure 9a compares mean reflectances from clear footprints as identified by the ERBE MLE technique (Wielicki and Green 1989) with solar zenith angle, and Fig. 9b shows the corresponding relative differences between CERES and ERBS values [(CERES − ERBS)/ERBS × 100%]. In all cases, the CERES mean reflectances are lower than those of ERBS. Relative differences are as high as ≈9% for the full-resolution case but are only ≈2% for CERES (lowres). Also, the relative differences show little or no sensitivity to solar zenith angle. The drastic change in the CERES–ERBS reflectance difference with footprint size in Fig. 9b occurs because larger footprints identified as clear under the MLE technique suffer from greater cloud contamination than smaller footprints. That is, because there is a greater likelihood of encountering undetected subresolution cloud when the footprint size is large, it becomes much more difficult to identify cloud-free footprints unambiguously. Consequently, CERES clear-sky SW reflectances tend toward ERBE clear-sky values when footprint size differences between the two instruments are removed.

Relative differences between CERES and ERBS SW reflectances for other surface types are provided in Table 8 for both full-resolution and spatially averaged CERES footprints. Results for scenes identified as clear and overcast are shown together with the ''all-sky'' difference inferred from averages obtained by considering all observed CERES and ERBS footprints between 20°N and 20°S. To identify cold deep convective clouds, the approach outlined in Currey and Green (1999) was used. Also shown in Table 8 are differences between reflectances obtained when both CERES and ERBS reflectances are unfiltered using the technique outlined in section 2b [Eq. (3)]. Overall, the ERBS all-sky SW radiances were found to increase by ≈1.6% using the new technique. The last column in Table 8 provides an estimate of the natural variability in the CERES–ERBE relative differences determined from the 95% confi-

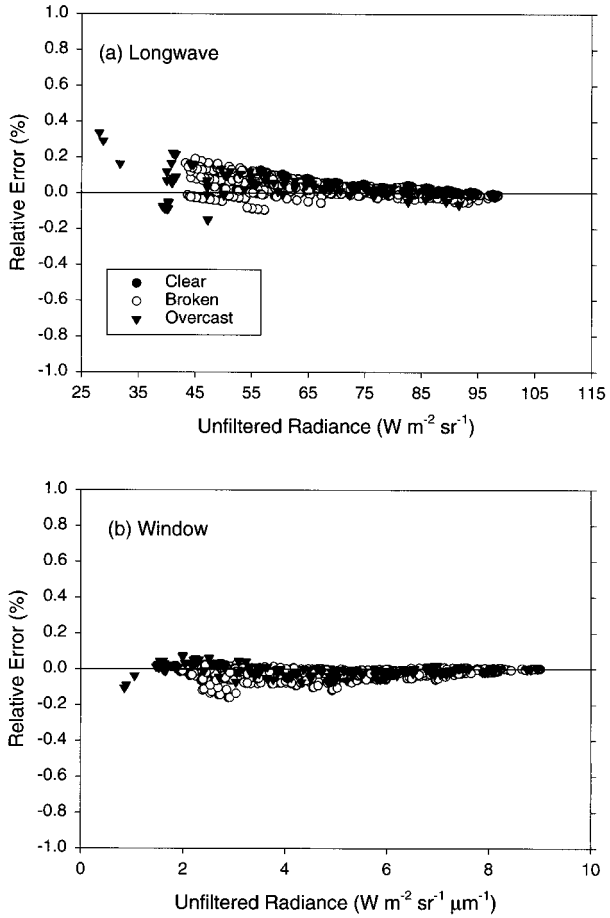

FIG. 5. Relative error in unfiltered (a) LW and (b) WN radiance estimate against the true unfiltered radiance for clear, broken, and overcast scenes over ocean.

dence interval (relative to the mean reflectance) from 5 yr of ERBS JJA SW reflectances for each scene type. For the individual scene types, relative differences between CERES and ERBS range from $\approx -8.8\%$ to $\approx 2.2\%$ for the CERES (fullres) case, as compared with $\approx -4.7\%$ to $\approx -1.0\%$ for the CERES (lowres) case. Not surprisingly, CERES footprint size has a much smaller influence on SW reflectances over brighter surfaces such as clear land and desert than it does over clear ocean. When both ERBS and CERES data are unfiltered using the same technique [i.e., based on Eq. (3)], relative differences show much less dependence on scene type, ranging between $\approx -4.7\%$ and $\approx -3.4\%$ for the individual scenes. The all-sky relative differences in Table 8 (last row) are different from those for the individual scene types because of differences in the CERES and ERBS populations in these datasets. That is, because the relative frequency of occurrence of individual scene types is not exactly the same for CERES and ERBS, the overall mean reflectance from the two datasets is different, independent of errors caused by the unfiltering technique. Scene-type frequencies of occurrence for the ERBE scene types are shown in Table 9. Similar results to those in Tables 8 and 9 are obtained when all other viewing geometries are considered.

The $\approx -4.7\%$ to $\approx -3.4\%$ ($\approx -4\%$ on average) difference in SW reflectance between CERES and ERBS for individual scene types is surprisingly large. Because this difference shows very little sensitivity to scene type (i.e., when ERBS and CERES radiances are unfiltered using the same technique), the cause is likely not due to the unfiltering method. A more likely cause is calibration differences between CERES and ERBS.

Other factors that may complicate the comparison between CERES and ERBS include uncertainties in correcting for the thermal component of the ERBS SW channel (Green and Avis 1996), differences in sampling between CERES and ERBS, and the fact that the CERES–TRMM and ERBS measurements were recorded ≈ 10 yr apart, so that any changes in surface properties are unaccounted for.

b. LW radiance comparisons

Relative differences between CERES–TRMM and ERBS near-nadir LW radiances for the same period considered in section 4a are shown in Figs. 10a,b as a function of scene type for daytime (Fig. 10a) and nighttime (Fig. 10b) conditions. The CERES (lowres) radiances are compared with the original ERBS radiances (denoted by ''ERBS''), and the ERBS radiances unfiltered with the algorithm described in section 2b [denoted in the figure by ''ERBS (Eq. 3)'']. CERES LW radiances are within $\approx 0.1\%$ of ERBS values over clear ocean, and within $\approx 0.5\%$ over clear land and clear desert. The reason for the systematic decrease in daytime relative differences with increasing cloud cover is due to a bias in the shortwave portion of the TOT channel on ERBS. Green and Avis (1996) showed that, over 4 yr of ERBS scanner operation, the SW part of the TOT channel increased by $\approx 1.3\%$. This increase caused a 0.2% increase in daytime clear ocean LW fluxes and an increase of $\approx 2.6\%$ in LW fluxes for overcast scenes. This increase in ERBS radiances with cloud cover causes a decrease in CERES–ERBS relative differences.

Because of differences in the frequency of occurrence of individual scene types between CERES and ERBS (Table 9), the relative difference in the all-sky mean LW radiance is very large—during the daytime, all-sky LW radiances from CERES are $\approx 1.1\%$ higher than ERBS archived values; at night, CERES radiances are higher by $\approx 2.1\%$. Applying the unfiltering algorithm proposed in section 2b to the ERBS data reduces the CERES–ERBE relative differences for most scene types. The relative difference for the all-sky case is now $\approx 0.6\%$ during the daytime but remains high at night ($\approx 1.9\%$). Note that the daytime relative difference is likely too low because of the overestimate in the ERBS daytime LW radiance caused by the error in the ERBS SW part of the TOT channel. If this were corrected, the CERES–

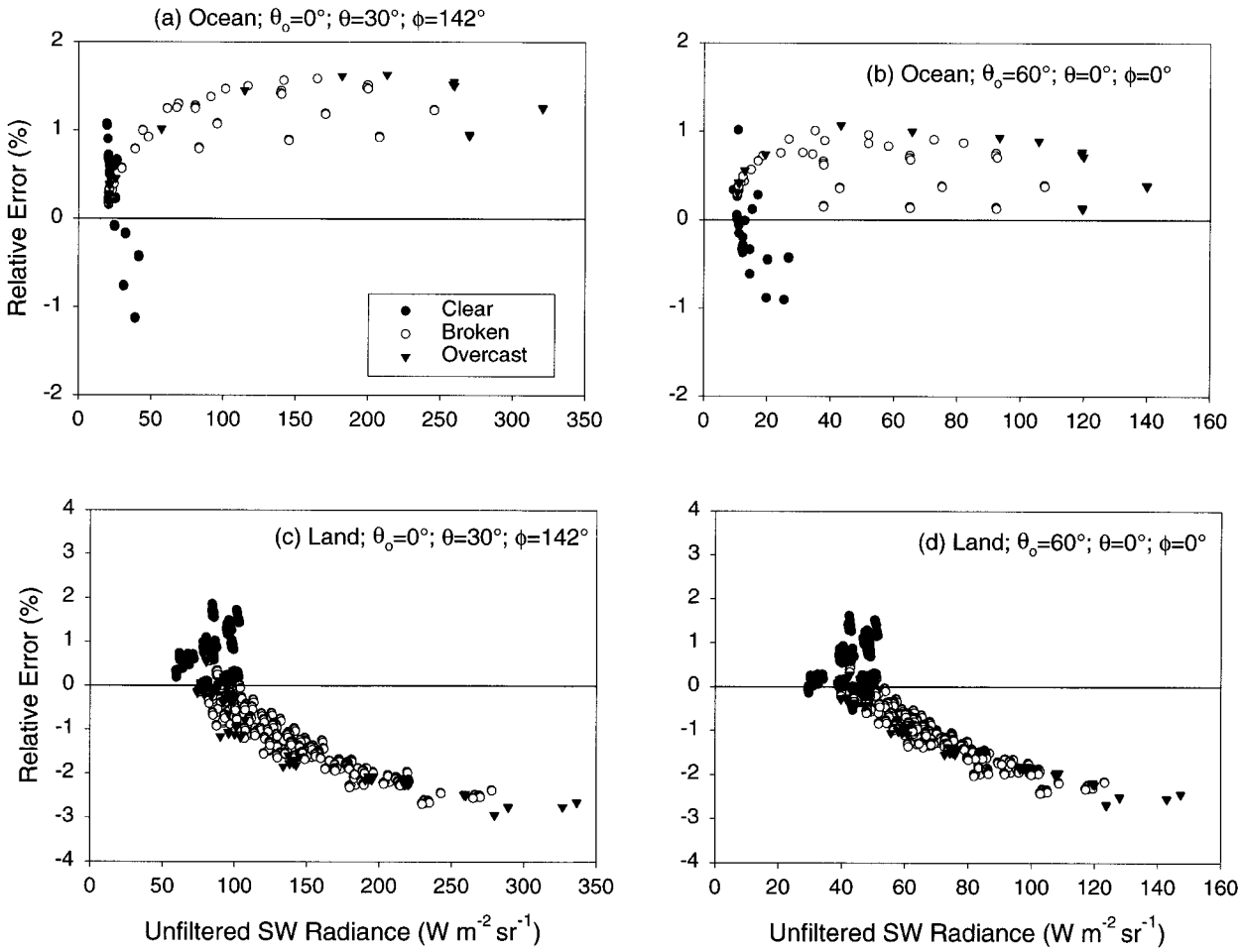

FIG. 6. Relative error in unfiltered SW radiance estimate for the same cases as in Fig. 4 but where the unfiltered SW radiances for clear scenes (''clear'') are determined using regression coefficients derived under cloudy conditions, and the unfiltered SW radiances for cloudy scenes (''broken'' and ''overcast'') are determined from regression coefficients derived under clear conditions.

ERBE daytime differences would be closer to ≈2%, consistent with the nighttime values.

5. Window channel radiance comparison with model calculations

In the absence of a window channel on ERBS, an alternate approach for validating unfiltered WN radiances is to compare CERES measurements with line-by-line radiative transfer calculations. Such a comparison was recently performed by Kratz et al. (2000, manuscript submitted to *J. Geophys. Res.*) for deep convective clouds (DCC). Figures 11a,b from that study show filtered TOT against filtered WN radiances (Fig. 11a) and unfiltered LW against unfiltered WN radiances (Fig. 11b) from line-by-line calculations and from CERES nighttime DCC measurements. The regressions utilized all occurrences of DCC from August of 1998. To identify DCC conditions, a filtered WN radiance threshold of 4 W m^{-2} sr^{-1} at nadir was used, which corresponds to a brightness temperature of ≈217 K. Theoretical simulations are based on a McClatchey (1972) tropical atmosphere and DCC parameterizations with cloud tops between 13 and 19 km. Several cloud optical depths and wavelength-dependent cloud extinction coefficients were considered. Theory and measurement are in very good agreement for both the filtered and unfiltered radiances in Figs. 11a,b. The line-by-line radiances are within ≈0.2% (1 std dev) of the filtered radiance measurements and within ≈0.4% (1 std dev) of the unfiltered measurements.

6. Summary

Broadband scanning radiometers measure filtered radiances, whereas most science applications of radiation budget data require radiances that do not depend on the optical path in the instrument. A method for unfiltering CERES radiance measurements that uses theoretically based regressions between filtered and unfiltered radiances for the CERES SW, LW, and WN channels was presented. In this method, regression coefficients are

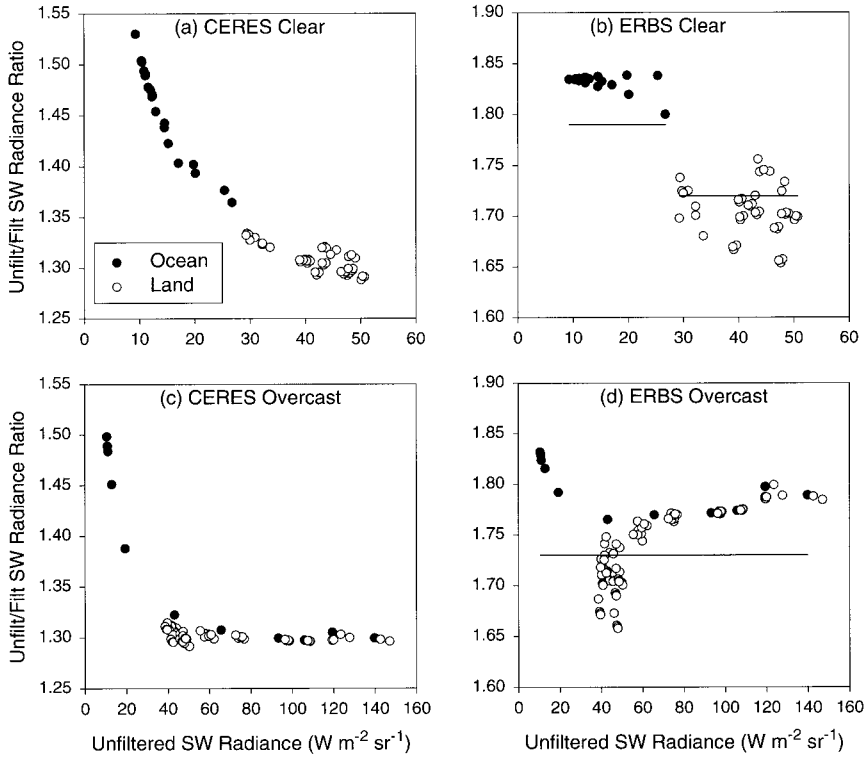

FIG. 7. Ratio of unfiltered to filtered SW radiances from theory against unfiltered radiance over ocean and land for (a) CERES clear, (b) ERBS clear, (c) CERES overcast, and (d) ERBS overcast. The solar zenith angle is 60°, and the viewing zenith angle is at nadir. Lines in Figs. 7b and 7d correspond to the unfiltering coefficients used in the ERBE production code.

stratified by viewing geometry and scene type. Scene types are determined by the surface type (ocean, land and desert, and snow) and whether cloud is present.

A detailed error analysis shows that instantaneous relative errors in the unfiltering procedure are generally well below 1% for SW radiances (std dev ≈0.4% or ≈1 W m^{-2} equivalent flux), except in the presence of very thin cirrus and in cloud-free conditions with large concentrations of submicron absorbing aerosols. For these cases, uncertainties are typically between ≈1% and 1.5%. For the LW channel, relative errors are generally less than ≈0.2% (std dev ≈0.1% or ≈0.3 W m^{-2} equivalent flux) except for very cold deep convective cloud cases, for which relative errors are closer to ≈0.4%. In the WN channel, relative errors are even smaller [<≈0.2% (std dev ≈0.1%)].

Because of large differences between CERES and ERBS spectral response functions, it is inappropriate to apply the ERBE method of unfiltering radiances (which is based on a single unfiltering ratio) to CERES. For ERBS, use of a single unfiltering ratio is less problematic over ocean, with errors remaining less than ≈4%. However, over land, the ERBS unfiltering ratio can vary by ≈6%–8%. Three months of CERES–TRMM unfiltered radiances from June, July, and August of 1998 between 20°S and 20°N were compared with ERBS scanner measurements for the same months over a 5-yr period (1985–89). To reduce scene identification errors, both datasets used the MLE technique (Wielicki and Green 1989) to identify the scene type. CERES frequency distributions of SW reflectance over ocean show good qualitative agreement with ERBS when CERES footprints are spatially averaged to the ERBS resolution. When compared with ERBS archived unfiltered SW reflectances, full-resolution CERES reflectances are ≈7.5% (≈3 W m^{-2} equivalent diurnal average flux) lower than ERBS over clear ocean as compared with ≈1.7% (≈4 W m^{-2} equivalent diurnal average flux) for deep convective clouds. When differences in footprint size between CERES and ERBS are accounted for, CERES values remain lower than ERBS by ≈<1%–2% (0.5–1.0 W m^{-2} equivalent diurnal average flux) for clear ocean and deep convective clouds, and ≈4.7% (≈2.5–3.5 W m^{-2} equivalent diurnal average flux) for clear land and desert. The scene type dependence in the difference is reduced further when the unfiltering scheme proposed in this study is applied to both CERES and ERBS. In that case, ERBS all-sky SW radiances increase by ≈1.7%, and CERES values are lower than the modified ERBS values by ≈3.4%–4.7% when the CERES footprints are spatially averaged to match ERBS. Further study is needed to determine the cause for the ≈4% difference between CERES and ERBS. At

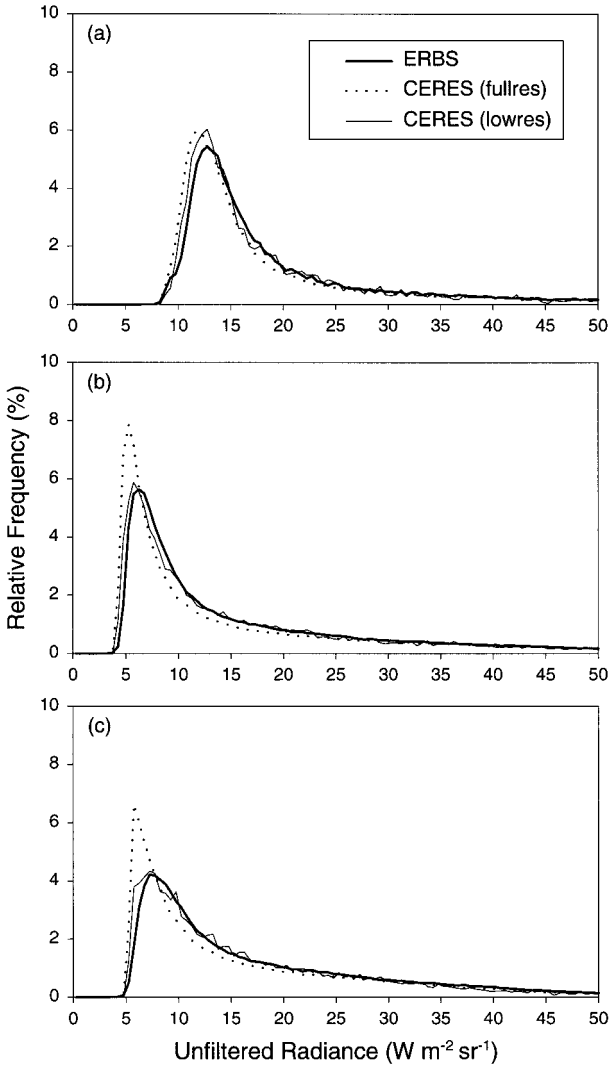

FIG. 8. Relative frequency distributions of near-nadir (viewing zenith angles ≤ 5°) SW reflectance for all scenes over ocean at solar zenith angles between (a) 5° and 10°, (b) 35° and 40°, and (c) 65° and 70°.

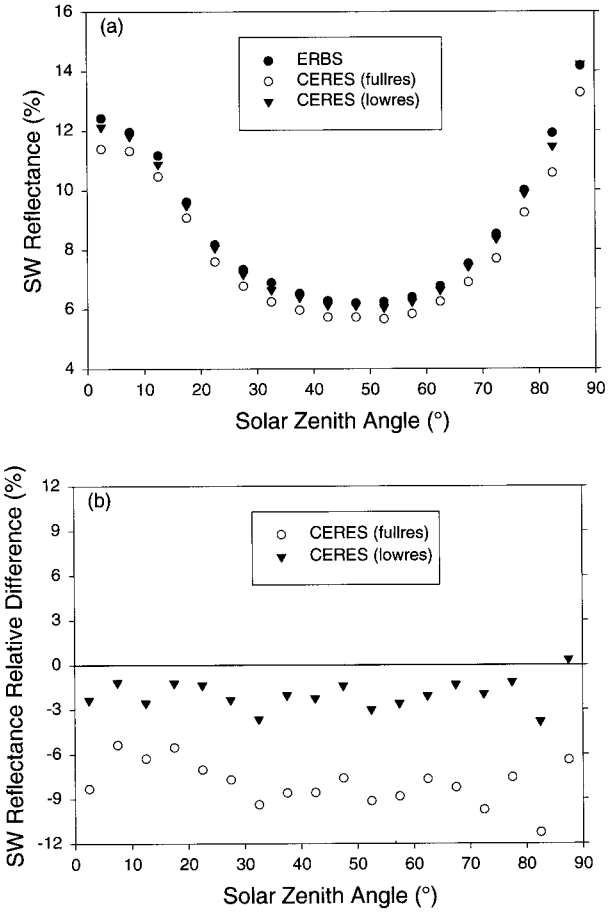

FIG. 9. (a) Mean reflectances from clear footprints as identified by the ERBE MLE technique against solar zenith angle; (b) relative differences between CERES and ERBS values in (a).

this stage, even calibration error cannot be ruled out as a possible cause.

CERES LW radiances are within ≈0.1% (≈0.3 W m^{-2}) of ERBS values over clear ocean and ≈0.5% (≈1.5 W m^{-2}) over clear land and desert. Under all-sky conditions, daytime LW radiances from CERES are ≈1.1% (≈3 W m^{-2}) higher than ERBS archived values; at night, CERES radiances are higher by ≈2.1% (≈5

TABLE 8. Relative difference in CERES–ERBS SW reflectance for viewing zenith angles ≤ 5°. The last column provides an estimate of the natural variability in the CERES–ERBE relative differences determined from the 95% confidence interval (relative to the mean reflectance) from 5 yr of ERBS JJA SW reflectances for each scene type.

Scene type	Relative difference (%)			ERBS 95% confidence interval relative to mean (%)
	CERES (fullres) − ERBS	CERES (lowres) − ERBS	CERES (lowres) − ERBS [Eq. (3)]	
Clear ocean	−7.5	−1.3	−3.4	3.7
Clear land	−6.4	−4.7	−3.4	4.0
Clear desert	−6.2	−4.6	−4.7	3.3
Clear land–ocean mix	−8.8	−2.5	−4.0	3.2
Overcast	2.2	−1.0	−3.6	1.9
Deep convective	−1.7	−1.7	−4.6	1.1
All-sky	−0.8	−0.8	−2.4	1.8

TABLE 9. CERES and ERBS scene-type frequency of occurrence for daytime and nighttime.

Scene type	Scene type frequency of occurrence (%)					
	Daytime			Nighttime		
	ERBS	CERES (fullres)	CERES (lowres)	ERBS	CERES (fullres)	CERES (lowres)
Clear ocean	18	25	23	12	17	18
Clear land	5	6	6	5	7	7
Clear desert	3	3	3	3	3	3
Clear land–ocean mix	1	2	1	0.7	1	1
Partly cloudy ocean	29	24	27	39	34	36
Partly cloudy land/desert	6	5	6	6	5	5
Partly land–ocean mix	2	1	2	2	2	2
Mostly cloudy ocean	17	15	14	16	13	13
Mostly cloudy land/desert	4	4	4	3	3	3
Mostly land–ocean mix	1	1	1	1	0.9	0.9
Overcast	14	14	13	12	16	10

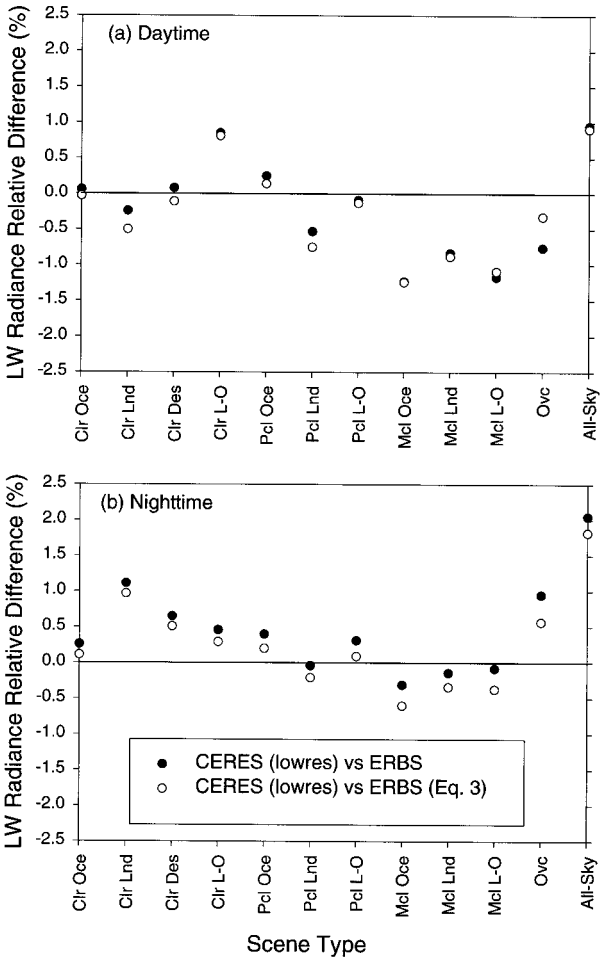

FIG. 10. Relative differences between CERES and ERBS near-nadir LW radiances as a function of scene type for (a) daytime and (b) nighttime conditions.

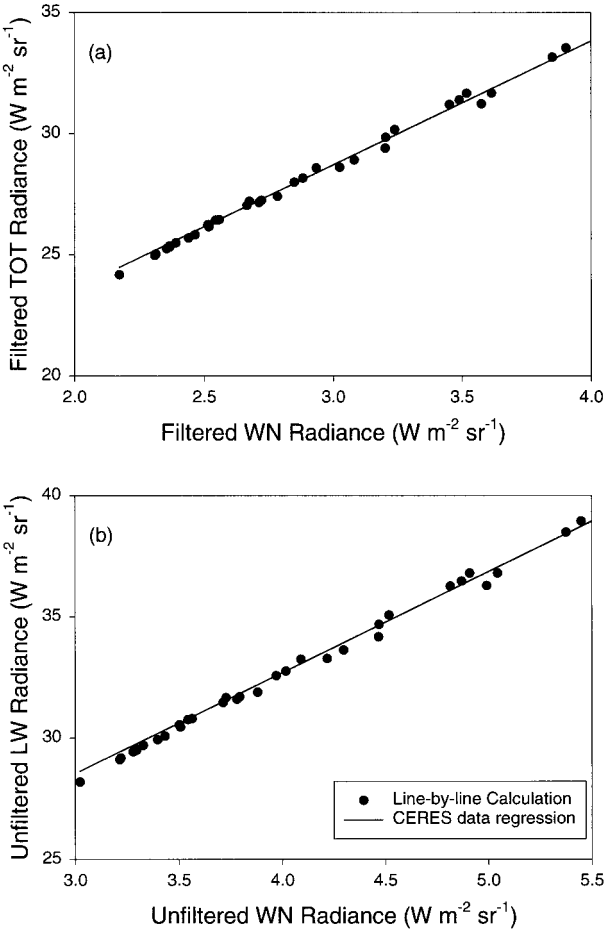

FIG. 11. Comparison between line-by-line radiative transfer model calculations and regressions of CERES radiance measurements of deep convective clouds. (a) Filtered TOT against filtered WN radiances; (b) unfiltered LW against unfiltered WN radiances.

W m^{-2}). When the CERES unfiltering approach is also used to unfilter ERBS LW radiances, the all-sky relative difference is reduced to ≈0.6% during the daytime, and remains high (≈1.9%) at night. The small daytime difference is attributable to an error in the shortwave part of the ERBS TOT channel. Comparisons between CERES measurements and line-by-line model calculations of WN and LW radiances are found to be consistent to within ≈0.4%.

Acknowledgments. The authors thank Dr. Bruce R. Barkstrom for his insightful comments. This research was supported by NASA Grant NAG-1-1963.

REFERENCES

Arduini, R. F., 1985: Solar radiance models for determination of ERBE scanner filter factor. Contractor Rep. 172595, 40 pp. [Available from NASA Langley Research Center, MS 420, Hampton, VA, 23681.]

Barkstrom, B. R., 1984: The Earth Radiation Budget Experiment (ERBE). *Bull. Amer. Meteor. Soc.,* **65,** 1170–1186.

——, and G. L. Smith, 1986: The Earth Radiation Budget Experiment: Science and implementation. *Rev. Geophys.,* **24,** 379–390.

Bowker, D. E., R. E. Davis, D. L. Myrick, K. Stacy, and W. T. Jones, 1985: Spectral reflectances of natural targets for use in remote sensing studies. NASA Reference Publication, Rep. RP-1139, 184 pp.

Colwell, R. N., 1983: *Manual of Remote Sensing.* 2d ed. American Society of Photogrammetry, The Sheridan Press, 2440 pp.

Cox, C., and W. Munk, 1954: Some problems in optical oceanography. *J. Mar. Res.,* **14,** 63–78.

Currey, C., and R. N. Green, 1999: Validation of the CERES shortwave measurements over desert and cloud scenes. *Proc. 10th Conf. on Atmospheric Radiation,* Madison, WI, Amer. Meteor. Soc., 567–570.

Green, R. N., and L. M. Avis, 1996: Validation of ERBS scanner radiances. *J. Atmos. Oceanic Technol.,* **13,** 851–862.

JPL, 1998: ASTER Spectral Library Version 1.0. [Available online at http://speclib.jpl.nasa.gov/.]

Kneizys, F. X, and Coauthors, 1996: The MODTRAN 2/3 Report and LOWTRAN 7 Model. Phillips Laboratory, Geophysics Directorate, Hanscom AFB, MA, 261 pp. [Available from Phillips Laboratory, Geophysics Directorate, Hanscom AFB, MA 01731.]

Kriebel, K. T., 1978: Measured spectral bidirectional reflection properties of four vegetated surfaces. *Appl. Opt.,* **17,** 253–259.

Loeb, N. G., P. O'Rawe Hinton, and R. N. Green, 1999: Top-of-atmosphere albedo estimation from angular distribution models: A comparison between two approaches. *J. Geophys. Res.,* **104,** 31 255–31 260.

McClatchey, R. A., R. W. Fenn, J. E. A. Selby, P. E. Volz, and J. S. Garing, 1972: Optical properties of the atmosphere. 3d ed. AFCRL-72-0497, Environmental Research Papers No. 411, Air Force Cambridge Research Papers, Bedford, MA, 103 pp. [Available from Air Force Cambridge Research Laboratories, Bedford, MA 01730.]

Priestley, K. J., B. R. Barkstrom, H. Bitting, R. B. Lee III, D. K. Pandey, S. Thomas, and K. L. Thornhill, 1998: End-to-end spectral characterization of the Clouds and the Earth's Radiant Energy System (CERES) thermistor bolometers. *Proc. SPIE,* **3498,** 12–22.

——, and Coauthors, 2000: Postlaunch radiometric validation of the Clouds and the Earth's Radiant Energy System (CERES) proto-flight model on the Tropical Rainfall Measuring Mission (TRMM) spacecraft through 1999. *J. Appl. Meteor.,* **39,** 2249–2258.

Satheesh, S. K., V. Ramanathan, X. Li-Jones, J. M. Lobert, I. A. Podgorny, J. M. Prospero, B. N. Holben, and N. G. Loeb, 1999: A model for the natural and anthropogenic aerosols over the tropical Indian Ocean derived from INDOEX data. *J. Geophys. Res.,* **104,** 27 421–27 440.

Shettle, E. P., and R. W. Fenn, 1979: Models of the aerosols of the lower atmosphere and the effects of humidity variations on their optical properties. Report No. AFGL-TR-79-0214, Hanscom, MA, 94 pp. [Available from Phillips Laboratory, Geophysics Directorate, Hanscom AFB, MA 01731.]

Silverman, B. A., and E. D. Sprague, 1970: Airborne measurement of in-cloud visibility. Preprints, *Second National Conf. on Weather Modification,* Santa Barbara, CA, Amer. Meteor. Soc., 271–276.

Stamnes, K., S.-C. Tsay, W. Wiscombe, and K. Jayaweera, 1988: Numerically stable algorithm for discrete-ordinate-method radiative transfer in multiple scattering and emitting layered media. *Appl. Opt.,* **24,** 2502–2509.

Takashima, T., 1985: Polarization effect on radiative transfer in planetary composite atmospheres with interacting interface. *Earth Moon Planets,* **33,** 59–97.

Tarnopolskiy, V. I., 1978: Optical characteristics of the earth's surface and atmosphere from the point of view of remote sensing of natural surfaces. NASA Rep. TM-75548, 56 pp.

Wielicki, B. A., and R. N. Green, 1989: Cloud identification for ERBE radiation flux retrieval. *J. Appl. Meteor.,* **28,** 1133–1146.

——, B. R. Barkstrom, E. F. Harrison, R. B. Lee III, G. L. Smith, and J. E. Cooper, 1996: Clouds and the Earth's Radiant Energy System (CERES): An Earth Observing System experiment. *Bull. Amer. Meteor. Soc.,* **77,** 853–868.

Wiscombe, W. J., and S. G. Warren, 1980: A model for the spectral albedo of snow. I: Pure snow. *J. Atmos. Sci.,* **37,** 2712–2733.

Young, D. F., P. Minnis, D. R. Doelling, G. G. Gibson, and T. Wong, 1998: Temporal interpolation methods for the Clouds and the Earth's Radiant Energy System (CERES) experiment. *J. Appl. Meteor.,* **37,** 572–590.